JGR Planets

RESEARCH ARTICLE
10.1029/2019JE006209

Key Points:
- A poroviscoelastic model is developed to explore the interaction between permeable flow and rock deformation during tidal deformation
- The poroviscoelastic core generates more heat in both the fluid and solid component, compared to a solid viscoelastic core
- For certain permeabilities and viscosities, the total heating rate reaches 25–40 GW, similar to the observed value

Correspondence to:
Y. Liao,
yliao@whoi.edu

Citation:
Liao, Y., Nimmo, F., & Neufeld, J. A. (2020). Heat production and tidally driven fluid flow in the permeable core of Enceladus. *Journal of Geophysical Research: Planets*, *125*, e2019JE006209. https://doi.org/10.1029/2019JE006209

Received 16 SEP 2019
Accepted 22 JUL 2020
Accepted article online 28 JUL 2020

Heat Production and Tidally Driven Fluid Flow in the Permeable Core of Enceladus

Yang Liao[1], Francis Nimmo[2], and Jerome A. Neufeld[3,4,5]

[1]Department of Geology and Geophysics, Woods Hole Oceanographic Institution, Woods Hole, MA, USA, [2]Department of Earth and Planetary Sciences, University of California, Santa Cruz, CA, USA, [3]BP Institute, University of Cambridge, Cambridge, UK, [4]Department of Earth Sciences, University of Cambridge, Cambridge, UK, [5]Department of Applied Mathematics and Theoretical Physics, University of Cambridge, Cambridge, UK

Abstract Saturn's moon Enceladus has a global subsurface ocean and a porous rocky core in which water-rock reactions likely occur; it is thus regarded as a potentially habitable environment. For icy moons like Enceladus, tidal heating is considered to be the main heating mechanism, which has generally been modeled using viscoelastic solid rheologies in existing studies. Here we provide a new framework for calculating tidal heating based on a poroviscoelastic model in which the porous solid and interstitial fluid deformation are coupled. We show that the total heating rate predicted for a poroviscoelastic core is significantly larger than that predicted using a classical viscoelastic model for intermediate to large ($>10^{14}$ Pa·s) rock viscosities. The periodic deformation of the porous rock matrix is accompanied by interstitial pore fluid flow, and the combined effects through viscous dissipation result in high heat fluxes particularly at the poles. The heat generated in the rock matrix is also enhanced due to the high compressibility of the porous matrix structure. For a sufficiently compressible core and high permeability, the total heat production can exceed 10 GW—a large fraction of the moon's total heat budget—without requiring unrealistically low solid viscosities. The partitioning of heating between rock and fluid constituents depends most sensitively on the viscosity of the rock matrix. As the core of Enceladus warms and weakens over time, pore fluid motion likely shifts from pressure-driven local oscillations to buoyancy-driven global hydrothermal convection, and the core transitions from fluid-dominated to rock-dominated heating.

Plain Language Summary Discoveries made by the Cassini spacecraft revealed that we may find life even in our own cosmic neighborhood in the ocean of Saturn's moon Enceladus. Recent studies infer that the fluid-saturated rocky core of Enceladus harbors some of the processes that likely gave rise to life on Earth. Here we develop a physics-based model to understand the heating in the water-saturated porous core of Enceladus during periodic deformation under tidal forces. We find that the periodically loaded moon distributes the heat generated during its deformation in both its rocky and fluid part. When the core is strong and rigid (likely in the early history), heating in the fluid could be hundreds or thousands of times larger than that in the solid rock; when the core is severely weakened (such as in its later history), more heat is distributed in the solid rock than in the fluid. We also find that the coupling between pore fluid and solid rock may enhance the heating of the core for a larger range of material properties, in contrast with earlier studies. The enhanced heating could provide explanation for the high heat flux measured for Enceladus, and a potential hot period in its early history.

1. Introduction

In nearly 15 years after the discovery of the enigmatic polar plumes by Cassini (Porco et al., 2006), the interior structure and orbital history of Enceladus has been made clearer based on analysis of its gravity, topography and libration data, and numerical simulation (Iess et al., 2014; Neveu & Rhoden, 2019; Nimmo et al., 2018; Taubner et al., 2015; Vance et al., 2018). It is now believed that under the ice shell of the moon, there is a global, salty, liquid ocean (Čadek et al., 2016; Postberg et al., 2009, 2011, 2018; Thomas et al., 2016) overlying a highly porous, silicate-based rocky core (Hemingway et al., 2018; Iess et al., 2014; Roberts, 2015), where water-rock hydration reactions and hydrothermal circulation are supported (Choblet et al., 2017; Hsu et al., 2015; Sekine et al., 2015; Travis & Schubert, 2014; Waite et al., 2017)—a picture that presents great similarities to Earth (Kelley et al., 2005; Russell et al., 2010).

Enceladus is thought to consist of an ice shell about 20 km thick on average, overlying an ocean about 40 km deep and a low-density (≈2,500 kg m^{-3}), high-porosity rocky core (Čadek et al., 2016; Hemingway & Mittal, 2019; Iess et al., 2014). The shell is thinnest at the active south pole and also exhibits reduced thickness at the north pole (e.g., Hemingway & Mittal, 2019). Based on these thickness estimates, the total conductive heat loss across the whole of Enceladus is about 25–40 GW, while the measured excess thermal emission at the south pole is 16 ± 3 GW (Howett et al., 2011).

The source of the heat is Enceladus's tides, which transfer energy from Saturn's rotation. But the distribution of the tidal heating is currently uncertain. As previously reviewed (Nimmo et al., 2018), initial models (Roberts & Nimmo, 2008; Ross & Schubert, 1989; Shoji et al., 2013; Tobie et al., 2008) focused on dissipation in the ice shell. However, since the ice shell is thought to be conductive and the surface is cold, only a relatively thin layer at the base of the shell is warm enough to be dissipative. As a consequence, viscoelastic models have found it difficult to generate sufficient heat within the ice shell (Souček et al., 2019). Turbulent dissipation of water in south polar fractures could be an additional energy source (Kite & Rubin, 2016) but cannot explain the survival of relatively thin ice elsewhere, where fractures are absent (e.g., the northern polar region). Dissipation in the ocean driven by obliquity tides has been suggested as a major heat source (Tyler, 2009). However, for the inferred obliquity, and ocean and shell thicknesses, the magnitude of the predicted heat production is many orders of magnitude too small (Beuthe et al., 2016; Chen & Nimmo, 2011; Hay & Matsuyama, 2017; Matsuyama et al., 2018). Other mechanisms for driving turbulent ocean dissipation have also been suggested (Lemasquerier et al., 2017; Wilson & Kerswell, 2018) but have not so far received much scrutiny.

Recently, the silicate core has become more popular as a source of heat. A sufficiently weak silicate core can generate significant amounts of heat (Choblet et al., 2017; Efroimsky, 2018; Roberts, 2015). Below we consider an additional possibility: That tidal pumping of water through the porous core results in significant heat production. Tidally driven viscous dissipation in pore fluids can generate heat (Al-Hadhrami et al., 2003; Jupp & Schultz, 2004; Vance et al., 2007). For Enceladus, this mechanism has only been studied once in a simplified fashion (Vance et al., 2007) and was found to be insignificant in the context of heating and maintaining a liquid ocean. However, as that model omitted the interaction between porous fluid flow and tidal deformation, the resulting heating rates are likely underestimated.

Besides providing an additional heat source, heating of the fluid in the core of Enceladus is also relevant to geochemical processes crucial for understanding the habitability of the moon. On Earth, rock-water reactions and potential metabolic reactions under the seafloor need to occur in pore fluids and along the rock-fluid interface, where the motion and heating of pore water play a nonnegligible role (Mayhew et al., 2013; Schrenk et al., 2013; Schwarzenbach, 2016). Predicting the habitability beneath the seafloor of Enceladus therefore requires more knowledge of the thermal and kinetic history of the pore fluids and their relation with the rock matrix.

Currently, an explicit account of the coupling between porous flows and deforming rock matrix during tidal flexing is not achievable using either the commonly assumed viscoelastic description of tidal heating, or the poroelastic description of fluid motion (Choblet et al., 2017; Vance et al., 2007). As we explain below, both these end-member approaches neglect the coupling between porous solid and fluid, which can result in enhanced heating in both phases. A model for Enceladus that can evaluate the production of heat in both the pore fluid and rock matrix simultaneously and consistently has not been proposed hitherto.

In this paper, we propose a method of evaluating heating of the rock and pore fluid in the core by assuming a poroviscoelastic rheology, which consistently accounts for the coupling between pore fluid flows and deformation of the rock matrix. Our approach is simplified in that we assume a homogeneous poroviscoelastic spherical body loaded cyclically with an axisymmetric degree-2 pattern. In section 2, and in Appendices A and B, we provide the analytical framework for solving this simplified problem. In section 3 we compare our results for heat production in both the solid and fluid components with the end-member viscoelastic solution in which the pore fluid is neglected; we also explore the spatial pattern of heating. In section 4 we explore how the evolution of the mechanical properties of the core may have changed the dominant heat-producing mechanism over time. Finally, we conclude with a discussion of our results and a sketch of how a more complete analytical description may be accomplished.

2. Methods

2.1. Overview of the Model

The core of Enceladus is modeled as a poroviscoelastic, spherical body with uniform porosity, permeability, elastic moduli, and viscosity. The core is assumed to be submerged in an overlying ocean and all pore spaces are filled with fluid with constant viscosity. During tidal deformation, the solid rocks in the core deform periodically, generating heat (i.e., tidal heating). The deformation of the rock matrix causes the pore spaces to compress/dilate, driving porous fluid flows and generating heat via fluid dissipation. As redistribution of pore pressure changes the local stress and strain rate in the rock matrix, the coupling between fluid and solid components in our model is intrinsically two way. To obtain the heating rates, the model seeks analytical solutions for quantities including strain, stress, and velocity based on the assumptions and constraints below.

The core is assumed to have properties of both a viscoelastic (i.e., viscous relaxation of the rock matrix) and poroelastic material (i.e., mechanical coupling between pore pressure and total stress), which is described by linear poroviscoelastic constitutive relations. The constitutive relations explicitly couple the pore pressure and fluid mass with the strain and stress of the rock matrix (see next section). The motion of the interstitial fluids, driven by spatial gradients of fluid pore pressure, satisfies Darcy's law and mass conservation. The model assumes force balance while omitting the generation of seismic waves, leading to a quasi-static equilibrium condition for the total stress.

The quantitative framework is completed by boundary conditions and additional geometrical requirements of the solutions: At the surface of the core (i.e., seafloor), the fluid pressure and stress are continuous; at the poles of the core's surface, the amplitude of strain is approximated by a function of the moon's orbital motion and its degree-2 Love number determined by the rigidity and viscosity of the solid rock matrix (see next section); the model implicitly accounts for the gravitational potential caused by the moon's orbital motion by imposing degree-2 spatial geometries and periodicity of the solutions and through the imposed boundary conditions. The model is simplified by assuming only axisymmetric degree-2 geometry, ignoring longitudinal variations of gravitational potential.

2.2. Model Setup and Solutions

In this work we focus entirely on the water-filled silicate core of Enceladus. We largely neglect the role of the overlying ocean and ice shell. While these components will modify the tidal deformation of the core, the changes expected are small while greatly complicating the analytical development. Parameter values assumed are tabulated in Table A1.

In a poroviscoelastic material, the total stress is shared between pressurization of the pore fluid and the deformation of the rock matrix. In comparison to the classical Maxwell viscoelastic description commonly assumed for tidal heating models, a poroviscoelastic description incorporates an additional contribution of pore fluid pressure to the bulk rheology. Its constitutive relation can be obtained by combining classical linear poroelasticity and a Maxwell viscoelastic model wherein viscous relaxation occurs in the shear components (Biot, 1941; Cheng, 2016; Rice & Cleary, 1976; Roberts & Nimmo, 2008; Tobie et al., 2005; Wu & Peltier, 1982),

$$\frac{\partial \sigma}{\partial t}+\frac{\mu}{\eta_m}\sigma-\frac{1}{3}\frac{\mu}{\eta_m}Tr(\sigma)I=2\mu\frac{\partial \epsilon}{\partial t}+\left(K_m-\frac{2}{3}\mu\right)\frac{\partial Tr(\epsilon)}{\partial t}I-\alpha\frac{\partial P}{\partial t}I. \tag{1}$$

Here $\sigma(r, \theta, t)$ and $\epsilon(r, \theta, t)$ are the stress and strain tensors for the ensemble material, $P(r, \theta, t)$ is the pore pressure, I is a unit tensor, and μ and η_m are the rigidity (i.e., shear modulus) and viscosity of the rock matrix. The poroelastic coefficient α (also known as the Biot constant) indicates the relative strength of the rock matrix in comparison with that of pure rock and has a value between 0 and 1, and $K_m=(1-\alpha)K_s$ is the bulk modulus of the rock matrix where K_s is the bulk modulus assumed for pure rock. In the current study we assume $K_s=10$ GPa or smaller, according to values assumed for Earth's oceanic crust (Crone & Wilcock, 2005; Vance et al., 2007). We can verify that the Maxwell formulation in classical tidal heating studies can be obtained from Equation 1 when the pore pressure is decoupled from the matrix with $\alpha=0$ (Brusche & Sundermann, 1978; Peale & Cassen, 1978; Ross & Schubert, 1989; Segatz et al., 1988; Tobie et al., 2005;

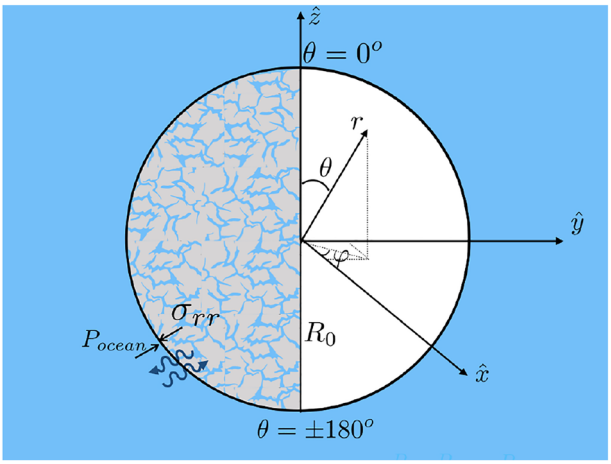

Figure 1. Setup of the axisymmetric model. The core of Enceladus is modeled as a spherical, homogeneous poroviscoelasitic body with radius R_0. The body undergoes axisymetric oscillation with a period of 33 hours. During periodic deformation, all quantities depend on radial position r and angle θ (measured from vertical axis) and are independent of azimuthal angle φ. Lower left quarter shows a fluid-loading condition, where fluid pressure is continuous on the surface, and internal stress balances with loading pressure.

Wu & Peltier, 1982). We implicitly assume that the bulk viscosity of the rock matrix is infinitely large in comparison with the shear viscosity η_m; hence, the viscous relaxation process only occurs in the shear component, similar to previous studies.

The core of Enceladus is modeled as a spherical, homogeneous, poroviscoelastic body under a fluid-loading boundary condition at its surface (see Figure 1). Following earlier works, we assume irrotational deformation with displacement $\vec{u} = \nabla\Phi$ (Landau & Lifshitz, 1959; Love, 1927), where the displacement potential $\Phi(r, P_2(\theta))$ is axisymmetric and has a degree-2 pattern in zonal direction (P_2 is degree-2 Legendre polynomial with $m = 0$). As discussed below, this is a simplification of the actual tidal pattern, which includes both P_2^0 and P_2^2 components for eccentricity tides (e.g., Tobie et al., 2005). Under periodic loading, all the quantities in the system (denoted by f here) are represented by complex amplitudes as $f = Re(\hat{f}(r, \theta)e^{i\omega t})$, where f stands for strain, stress, pore pressure, or fluid velocity; $\hat{f}$ is the complex amplitude of f; and ω is the loading frequency. The constitutive relations, equilibrium condition, Darcy's law and pore fluid continuity lead to analytical solutions for the displacement potential and the pore pressure (see Appendices A and B for derivation)

$$\hat{\Phi} = -\frac{\alpha C_1}{k^2\left(K_m + \frac{4}{3}\mu^*\right)}\left(3\frac{\sin kr}{k^3r^3} - 3\frac{\cos kr}{k^2r^2} - \frac{\sin kr}{kr}\right)(3\cos 2\theta + 1) + C_2 r^2(3\cos 2\theta + 1), \tag{2}$$

$$\hat{P} = C_1(3\cos 2\theta + 1)\left(3\frac{\sin kr}{k^3r^3} - 3\frac{\cos kr}{k^2r^2} - \frac{\sin kr}{kr}\right),$$

where k is a complex wavenumber determined by material properties. In the present study, contributions from self-gravity and the tidal forcing from orbital eccentricity are considered in a simplified fashion and are implicitly reflected by the constant values of C_1 and $C_2 \propto C_1$, which are determined by the boundary conditions at the surface of the core (see Appendices A and B). The expressions for the displacement potential and pore pressure in Equation 2 further lead to solutions for the strain $\hat{\epsilon}$, stress $\hat{\sigma}$, and Darcy's velocity $\hat{\vec{q}}$ (see Equation A9 in section A1). The volumetric heating rates averaged over one tidal period are therefore

$$h_{\text{tide}}(r, \theta) = \Sigma_{i,j}\frac{1}{T_\omega}\int_{nT_\omega}^{(n+1)T_\omega}\sigma_{ij}\frac{\partial\epsilon_{ij}}{\partial t}dt + \frac{1}{T_\omega}\int_{nT_\omega}^{(n+1)T_\omega}P_f\frac{\partial\zeta}{\partial t}dt, \tag{3}$$

$$h_{\text{vis}}(r, \theta) = \frac{1}{T_\omega}\int_{nT_\omega}^{(n+1)T_\omega}\frac{\eta_f}{\kappa}\vec{q}\cdot\vec{q}\,dt, \tag{4}$$

where $T_\omega = 33$ hr is the orbital period for application to Enceladus. The volumetric heating rate h_{tide} is generated in the rock matrix and is the counterpart of tidal heating in a solid viscoelastic body. The last term in Equation 3 arises from the compression/dilation of the pore fluid (ζ is the relative amount of pore fluid entering the pore space) and typically has a negligible contribution. In Equation 4, h_{vis} represents the viscous heat generated in the pore fluid. The global heating rates in solid or fluid are $H_{\text{tide,vis}} = 2\pi\int_0^{R_0}\int_0^{\pi} h_{\text{tide,vis}}r^2\sin\theta d\theta dr$ and the total heating rate $H_{\text{total}} = H_{\text{tide}} + H_{\text{vis}}$. Under the boundary conditions of force balance and fluid pressure continuity at the surface of the core (i.e., the fluid-loading boundary condition; see Appendices A and B), the ratio $H_{\text{vis}}/H_{\text{tide}}$ is determined and represents the partitioning of total heat between the solid and fluid constituent in the core. To obtain the magnitude of the heating rates, an additional boundary condition is required to constrain C_1 and C_2.

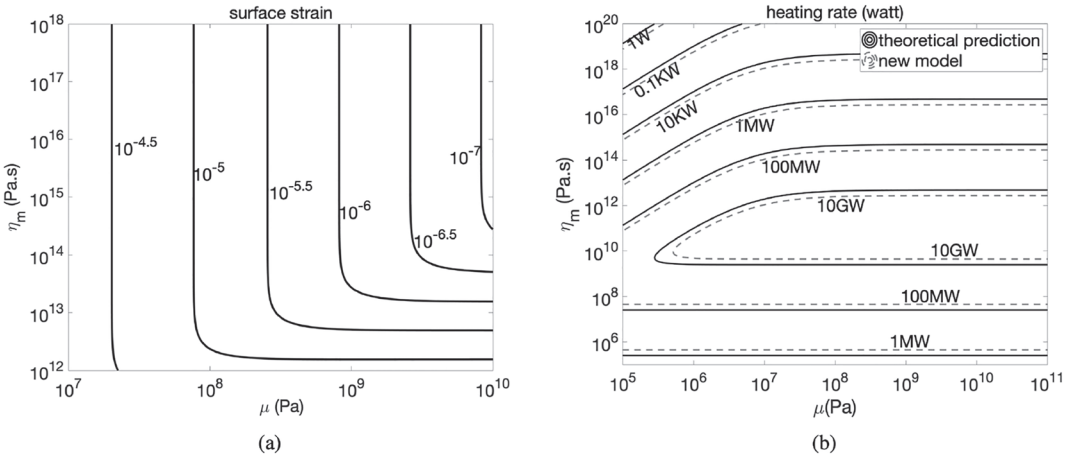

Figure 2. (a) Contours of polar strain amplitude assumed for the study $\epsilon_0 = \frac{9}{4\pi} e \frac{\omega^2}{\rho G} \frac{5}{3} |k_2^*|$ shown as a function of matrix viscosity and rigidity. The degree-2 Love number for a uniform body is $k_2^* = \frac{3/2}{1 + 19\mu^*/2\rho g R}$, where μ^* is the complex rigidity (see text). (b) Contours of tidal heating rate computed from theoretical prediction (black lines) $H_{\text{theory}} = -\frac{21}{2} \frac{\omega^5 R^5}{G} e^2 Im(k_2^*)$ and tidal heating rate for a viscoelastic end-member H_{visco} computed with the poroviscoelastic model with simplified, axisymmetric degree-2 potential, which is based on a boundary condition shown in (a). Our predicted heating using the simplified degree-2 potential is approximately 57% of the theoretical prediction.

In practice, the deformation of the porous core is forced by tidal variations in the gravitational potential, with the surface of the core treated as an interface with displacement and stress coupled to the volumetric deformation and pressurization of the overlying ocean, which in turn is coupled to ice shell deformation. Such complexities are beyond the scope of the present study. Here we instead simplify the forcing and the boundary condition by assuming that the maximum strain at the poles is determined by the viscoelastic properties of the solid matrix in the core. This allows us to carry out a direct comparison between the heating in a standard viscoelastic body and the additional heating arising from porosity and fluid flow. For diurnal tides the maximum tidal strain $\epsilon_{\max} \approx 3e \frac{M}{m} \frac{R_0^3}{a^3} h_2$ (Murray & Dermott, 1999). Here e is eccentricity of the orbit, M and m are the mass of the planet and moon, R_0 is the radius of the moon and a the planet-satellite distance; we take $h_2 = \frac{5}{3} k_2$, which is the appropriate limiting behavior when rigidity dominates over gravity; k_2 is the tidal Love number. Following Kepler's law the relation further becomes $\epsilon_{max} = \frac{9}{4\pi} e \frac{\omega^2}{\rho G} \frac{5}{3} k_2$, $k_2 = \frac{3}{5} \frac{3/2}{1 + 19\mu^*/2\rho g R}$ assuming a uniform body, where the complex rigidity $\mu^* = \mu \frac{i\omega\tau}{1 + i\omega\tau}$ depends on the viscosity and rigidity of the matrix (e.g., Ross & Schubert, 1989). We assume that the amplitude of the radial strain at the polar surface is $\epsilon_0 = \epsilon_{max} = \frac{9}{4\pi} e \frac{\omega^2}{\rho G} \frac{5}{3} |k_2|$, which is used for constraining C_1 (Figure 2a and see the Appendices A and B).

2.3. Choice of Permeability and Viscosity

The material properties of the core are represented by four parameters: rock matrix rigidity μ, viscosity η_m, permeability κ, and poroelastic coefficient α, which by definition ranges from 0 to 1. We consider a range of high permeabilities and moderate to low rigidities and viscosities in our study. In earlier works, the permeability of Enceladus was assumed to be no more than 10^{-10}m^2, given the typical value of the permeability of the oceanic crust on Earth (Choblet et al., 2017; Vance et al., 2007). Furthermore, Choblet et al. (2017) concluded that the permeability of the core of Enceladus needed to be smaller than 10^{-12} m^2 for high-temperature hydrothermal circulation to occur, as suggested by the occurrence of silica nanoparticles.

In our work below we consider a wider range of possible permeability values based on the results of some recent studies on Earth's seafloor, which suggest that the permeability is likely higher. In one study on the Cocos plate, numerical simulations suggested that permeabilities of 10^{-10} and 10^{-8} m^2 for recharge and discharge portions of one outcrop yield the best match between simulations and heat flow measurements (Lauer et al., 2018; Winslow et al., 2013). Borehole measurements of large permeabilities, up to 10^{-8} m^2, and porosities, up to 10%, have also been made at some locations (Lauer et al., 2018; Winslow et al., 2013). Although the structure of Earth's oceanic crust (e.g., sediment layers) are different from that in the core of Enceladus, the characteristic permeability for the latter is anticipated to be of a similar order of magnitude or higher because of its high porosity. The density of the core inferred from gravity studies suggests a porosity of at least 20–30% (section 1), while some studies have assumed porosities of up to 50% extending into the center of the core (Choblet et al., 2017; Roberts, 2015; Vance et al., 2018). As a result, we postulate that κ is likely higher than the typical value for Earth's seafloor, and consider a range of permeability of $\kappa \in [10^{-12},10^{-7}]$ m^2 in our study.

In some early works, the rigidity and viscosity of the core of Enceladus were estimated based on the properties of solid rocks, with typical values of $\eta_m \sim 10^{20}$ Pa·s and $\mu \sim 100$ GPa, leading to predictions of very small heating rates (e.g., Roberts & Nimmo, 2008). Other studies proposed lower rigidities and viscosities based on the presence of porosity, rock alteration (e.g., serpentinization), or weakening of the core, which result in higher heating rates (Choblet et al., 2017; Efroimsky, 2018; Roberts, 2015). In the recent work by Choblet et al. (2017), 10–30 GW of tidal heating results from a weak core, with an effective shear modulus $\mu_{eff} = |\mu^*| \in [10^7,10^8]$ Pa and dissipation function $Q_\mu^{-1} = \frac{Im(\mu^*)}{|\mu^*|} \in [0.2, 0.8]$, which, in the context of Maxwell viscoelastic rheology, corresponds to a low viscosity $\eta_m = \frac{1}{\omega}\frac{\mu_{eff}}{Q_\mu^{-1}}$, that is, less than 10^{13} Pa·s, and a low rigidity $\mu = \frac{\mu_{eff}}{\sqrt{1-(Q_\mu^{-1})^2}}$, that is, between 0.01 and 0.1 GPa. These values are interpreted as a consequence of weakening by cyclic loading, which has been observed in experiments of cyclic loading tests of cohesive soils (Choblet et al., 2017). However, solid viscosities $<10^{13}$ Pa·s resemble those of ice near its melting temperature, rather than those typical of near-solidus solid rock values ($>10^{18}$ Pa·s). In our study, we assume a range of rigidities between 0.01 and 10 GPa, and a low- to moderate-viscosity range of 10^{12} to 10^{18} Pa·s to represent a moderately to severely weakened core.

3. Model Results

In this section we first compare our results with end-member viscoelastic tidal heating in which the effect of the pore fluid is ignored. We then investigate how the presence of pore fluid affects heat production in both the solid and fluid components. Finally, we investigate the spatial pattern of our tidal heating model.

3.1. Comparison With Classical Predictions for a Viscoelastic End-Member

When the pore fluid is decoupled from the deformation of the rock matrix ($\alpha = 0$ or $\kappa = 0$), the body becomes effectively viscoelastic and a heating rate H_{visco} can be obtained (see Appendix A2). H_{visco} corresponds to the viscoelastic end-member of the poroviscoelastic model, which can be benchmarked using the classical viscoelastic model. According to earlier studies, the theoretical heating rate predicted by the classical Maxwell model is $H_{theory} = -21\omega^5 R_0^5 e^2 Im(k_2)/2G$ (Segatz et al., 1988; Tobie et al., 2005; Zschau, 1978). In our approach, H_{visco} is determined by the loading frequency, rigidity, and viscosity (see Appendix A1). H_{visco} is comparable to the theoretical prediction $H_{\text{visco}} \approx 57\% H_{\text{theory}}$ for a wide range of rigidity and viscosity values (Figure 2b). Due to the neglect of the additional degree-2 harmonic in the poroviscoelastic model, H_{visco} is always smaller than H_{theory}. As our poroviscoelastic model can reproduce the main characteristics of the viscoelastic end-member, we consider our choice of geometry and boundary conditions to be justified for the purposes of this preliminary study.

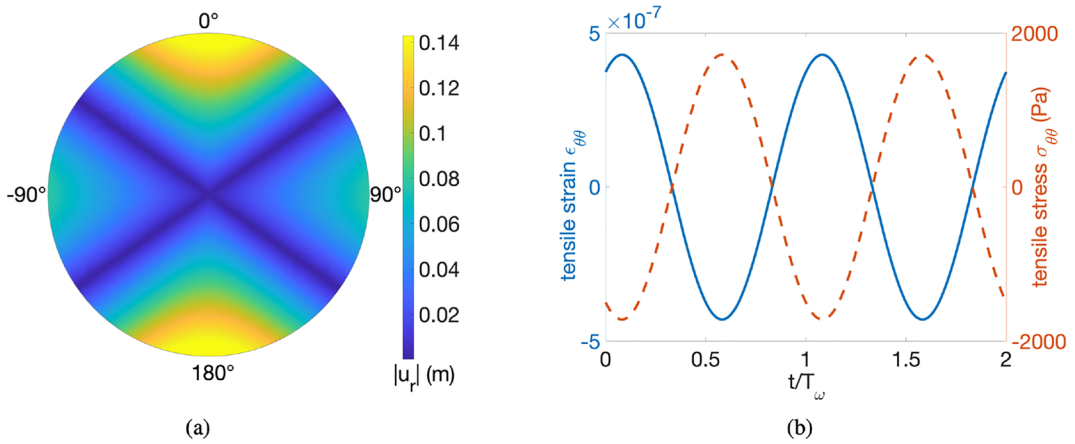

Figure 3. (a) The maximum magnitude of radial displacement $|\hat{u_r}|$ on a cross section of the spherical body. (b) The time series of tensile components of strain $\epsilon_{\theta\theta}$ and stress $\sigma_{\theta\theta}$ as functions of time measured under the north pole ($\theta = 0^o$) at depth 5.6 km below surface. The example case has permeability $\kappa = 1 \times 10^{-10}$ m^2, rock matrix rigidity $\mu = 1$ GPa, viscosity $\eta_m = 10^{17}$ Pa·s. Biot constant $\alpha = 0.2$.

3.2. Enhanced Heating and Heating Partition

During cyclic loading, the displacement in the poroviscoelastic body develops higher amplitudes at surface polar regions (Figure 3a). As in previous studies, phase lags exist between the stress and strain components, contributing to the generation of heat in the rock matrix (Figure 3b).

The coupling between the pore pressure and solid matrix allows for higher internal deformation relative to the viscoelastic end-member, causing the heating in the solid matrix to increase, even though the boundary strain remains small (determined by viscosity and rigidity). We find that the heating enhancement is especially prominent when the viscosity of the solid matrix is moderate or large: for example, at a rigidity of 1 GPa and viscosity of 10^{15} Pa·s, the total heating rate increases from 30 MW for the viscoelastic core to nearly 1 GW for the poroviscoelastic core when the poroelastic coefficient $\alpha = 0.9$, and to nearly 17 GW when $\alpha = 0.95$ and permeability 10^{-11} m^2 (Figure 4a). Since the total expected heat output of Enceladus is a few tens of GW (section 1), it is clear that poroviscoelastic dissipation in the core could supply a large fraction of Enceladus's total heat budget.

According to the micromechanical relation, $K_m = (1 - \alpha)K_s$ (K_m and K_s are the bulk moduli of the rock matrix (frame) and the pure rock, respectively), a large α indicates a much more compressible porous rock matrix in comparison to a purely solid rock. When $\alpha > 0.9$, the compressible rock matrix leads to a second heating rate peak that emerges at moderate matrix viscosity (Figure 4a). We consider that large values of α (>0.9) are likely, given the large porosity expected in the core of Enceladus. In the study of tidal pumping in the shallow crust of Enceladus by Vance et al. (2007), a frame bulk modulus of 0.1 GPa and rock bulk modulus of 10 GPa were assumed, corresponding to $\alpha \sim 0.99$ in the study. Although a large α likely exists for the porous core, it is not required for enhanced heating and the emergence of a second heating peak: with a lower value for $K_s < 2$GPa (e.g., caused by mineral alteration of water-rock reaction), even a moderate value of $\alpha < 0.8$ can lead to the same enhanced heating effect (see Figure B1a in Appendix B).

We further point out that the second heating peak (when it exists) occurs primarily in the solid component (see Figure B1b in Appendix B) and that the viscosity corresponding to the second heating peak varies primarily with the compressibility of the rock matrix (see Figures B1c and B1d in Appendix B). These observations suggest that the compressible rock matrix is the main contributor to the enhanced heating rate in the solid. As most tidal heating models assume an incompressible matrix, the effect of compressibility has not been extensively explored, although Hurford et al. (2006) explored the effects of varying material parameters including compressibility on the tidal response of the Earth. While Kaula (1964) found an increase in the heating rate of less than 3% when the compressibility of the lunar viscoelastic core was included, the enhanced heating rates, we observe here indicate that for a poroviscoelastic core, the compressible rock

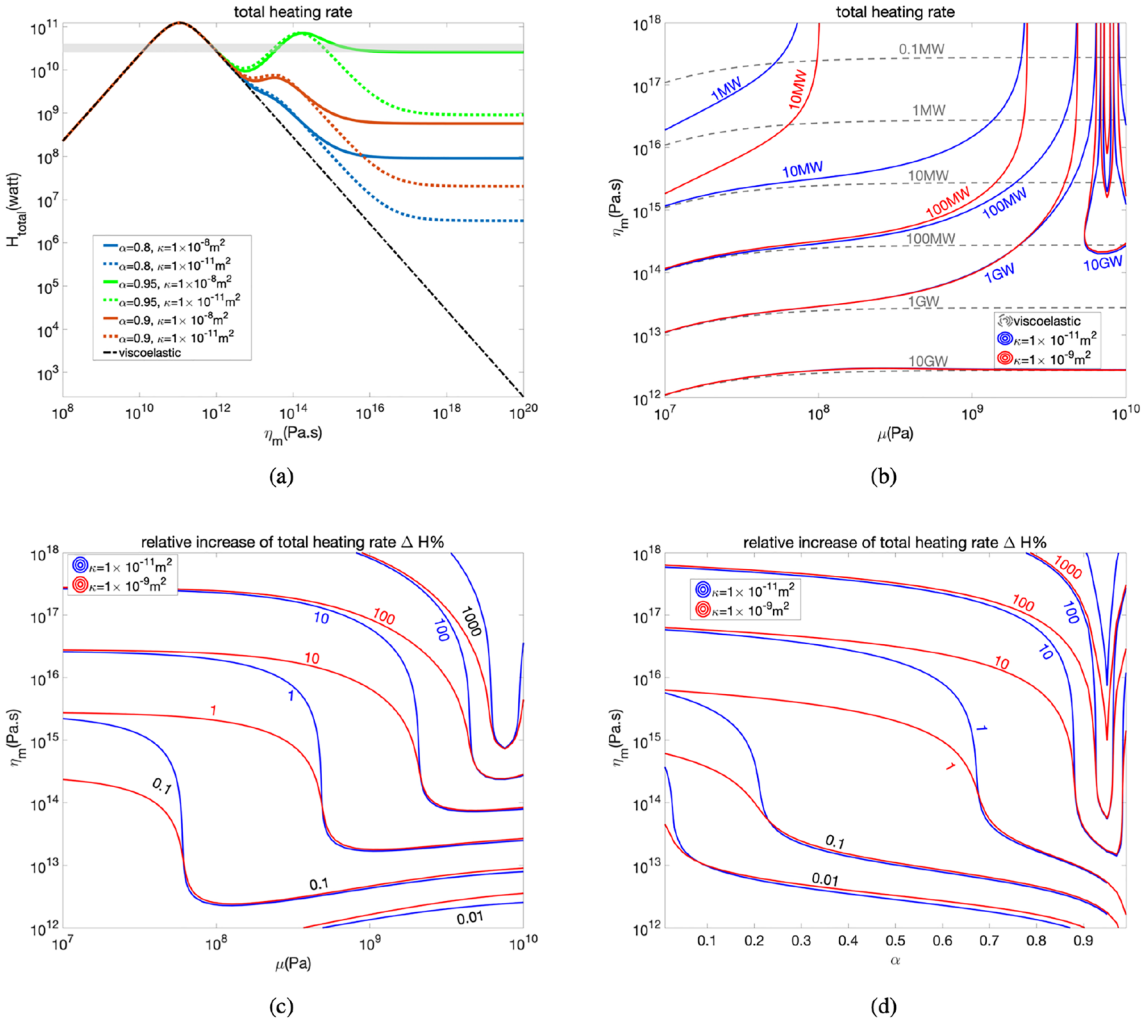

Figure 4. (a) The total heating rate $H_{total} = H_{tide} + H_{vis}$ as function of rock matrix viscosity for different poroelastic coefficient α and permeability κ, in comparison with the viscoelastic body (black broken line). For all cases, rigidity $\mu = 1$GPa, $K_s = 10$ GPa are assumed. The gray shaded box shows the estimated total heat flux for Enceladus (25–40 GW). (b) The contours of heating rate H_{total} as function of both rigidity and viscosity for two different permeabilities, for Biot constant $\alpha = 0.8$, $K_s = 10$ GPa. Gray dash lines indicate the viscoelastic counterpart. (c and d) The relative enhanced total heating $\Delta H\% = (H_{total} - H_{visco})/H_{visco}$, where H_{visco} is the heating rate of the viscoelastic counterpart with the same rigidity and viscosity. $\Delta H\%$ generally increases with η_m, μ, and α due to less effective viscoelastic dissipation under longer relaxation time, and more effective poroelastic diffusion under stronger coupling between pore pressure and matrix as α increases.

matrix and the subsequent coupling between the matrix with pore fluid pressure can influence the heating rate to a much larger extent than previously reported. Compressibility together with fluid permeability thus provides an alternative to ultralow solid viscosities as an explanation for high heat production rates in the core.

Besides enhanced heating in the solid component, the coupling between the rock and fluid phase causes fluid oscillation throughout the body, providing an additional heat source via viscous dissipation. The dissipative heating is especially prominent when the rock matrix viscosity and core permeability are moderate or high. At small (less than 10^{13} Pa·s) matrix viscosity, the poroviscoelastic core resembles the viscoelastic end-member, where viscoelastic deformation of the solid matrix dominates and the heating rates are consistent with the existing study by Choblet et al. (2017) (Figures 4a and 4b). Under the same boundary conditions, rigidity and rock viscosity, the total heating rate $H_{\mathrm{vis}} + H_{\mathrm{tidal}}$ for poroviscoslastic body is higher than that of the viscoelastic counterpart H_{visco}, with relative increase in heating rate $\Delta H_{\mathrm{total}}\%$

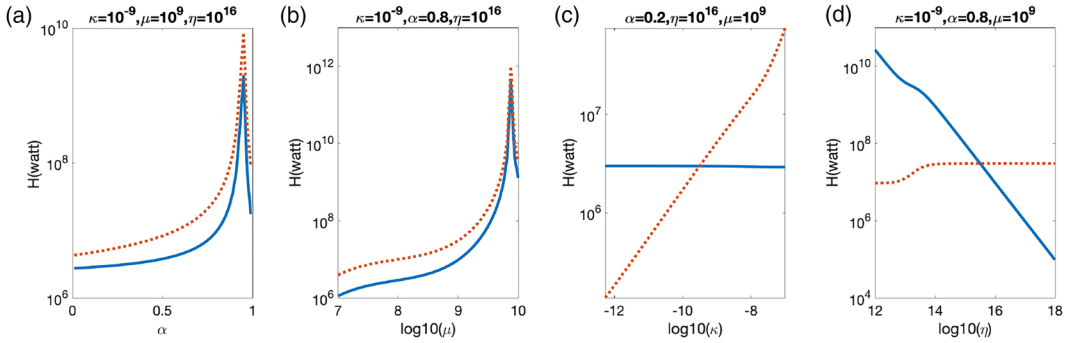

Figure 5. Tidal heating in solid matrix H_{tide} (blue solid lines) and viscous dissipation heating in pore fluid H_{vis} (red dash lines) as a function of (a) poroelastic coefficient α, (b) solid matrix rigidity μ, (c) permeability κ (H_{tide} is shown by left y axis), and (d) solid matrix viscosity η_m. Among the parameters κ and α affect poroelastic diffusion process, viscosity η_m affects the relaxation process, and rigidity μ effects both processes.

$= \dfrac{H_{\text{tidal}} + H_{\text{vis}} - H_{\text{visco}}}{H_{\text{visco}}}$ ranging from 1% for small viscosities ($\eta_m < 10^{14}$ Pa·s) to 1,000 times for large viscosities (see Figures 4c and 4d).

Both the heating rate of the solid rock H_{tide} and heating rate of the pore fluid H_{vis} vary with physical parameters including permeability, poroelastic coefficient, rigidity and viscosity (Figure 5). The dependence of H_{tide} on poroelastic parameters such as the permeability κ and poroelastic coefficient α indicates that heating in poroviscoelastic bodies is not a straight superposition of viscoelastic and poroelastic end-members, because of the interaction between poroelastic diffusion and viscoelastic relaxation processes. The partition of heat between the fluid component and solid component in the core is represented by the ratio $H_{\text{vis}}/H_{\text{tide}}$ and varies most sensitively with the viscosity of the matrix (see Appendix B Figure B2). Other parameters, including α, κ, and μ, only affect the partition of heat to a moderate degree.

Overall, for a moderately weakened or un-weakened rock with viscosity $\eta_m > 10^{16}$ Pa·s, most of the heat is produced in the pore fluid. For some choices of α and permeability, heat production rates can exceed 10 GW and thus contribute a significant fraction of Enceladus's global heat budget without requiring ultralow solid viscosities. For a severely weakened rock with viscosity $\eta_m < 10^{15}$ Pa, most of the heat is produced in the solid matrix. For a system with severely weakened rock (i.e., low viscosity) with strong tidal heating, as proposed in Choblet et al. (2017), the contribution of porous flow is very small. As a result, we postulate that the heat generated via porous flows was most likely to play a role before the core became severely weakened, most likely in the early history of Enceladus (see section 4 below).

3.3. Spatial Pattern of Heating

The volumetric heating rate $h_{\text{tide}}(r, \theta)$ and $h_{\text{vis}}(r, \theta)$ (Figures 6a–6f) for the poroviscoelastic body develop spatial patterns in response to fluid diffusion accompanying the cyclic deformation of the solid matrix. We find that the heating in the fluid phase h_{vis} concentrates below the seafloor under the polar regions and decreases with depth, with high heating rates focusing in a shallow layer with depth similar to the "skin depth" determined by poroelastic parameters (Jupp & Schultz, 2004; Vance et al., 2007) (see Appendix B). The heating in the solid matrix h_{tide} is virtually constant, with a small decrease toward the surface over the skin depth. This lack of spatial variation does not capture all the features of the classical model (Beuthe, 2013; Tobie et al., 2005), due to the missing harmonic modes in the deformation potential; therefore, although the simplified geometry is capable of reproducing the total heating rate, an accurate description of spatial distribution requires the inclusion of more harmonic modes. The volumetric heating rates lead to a rough estimation of the maximum surface heat flux, which is an integration of h_{tide} or h_{vis} in the radial direction. Due to our assumption of axisymmetric geometry, the resulting heat flux varies only with latitude at the surface of the core (Figures 6g–6i). For heat generated in the solid matrix, the flux peaks at mid latitude but is almost constant; for heat generated in the fluid, the heat flux peaks in the polar regions and is smallest at midlatitudes. We note in particular that panels (h) and (i) show peak polar heat fluxes of roughly 280 and 100 mW m^{-2}, enough to account for the measured polar flux (Howett et al., 2011).

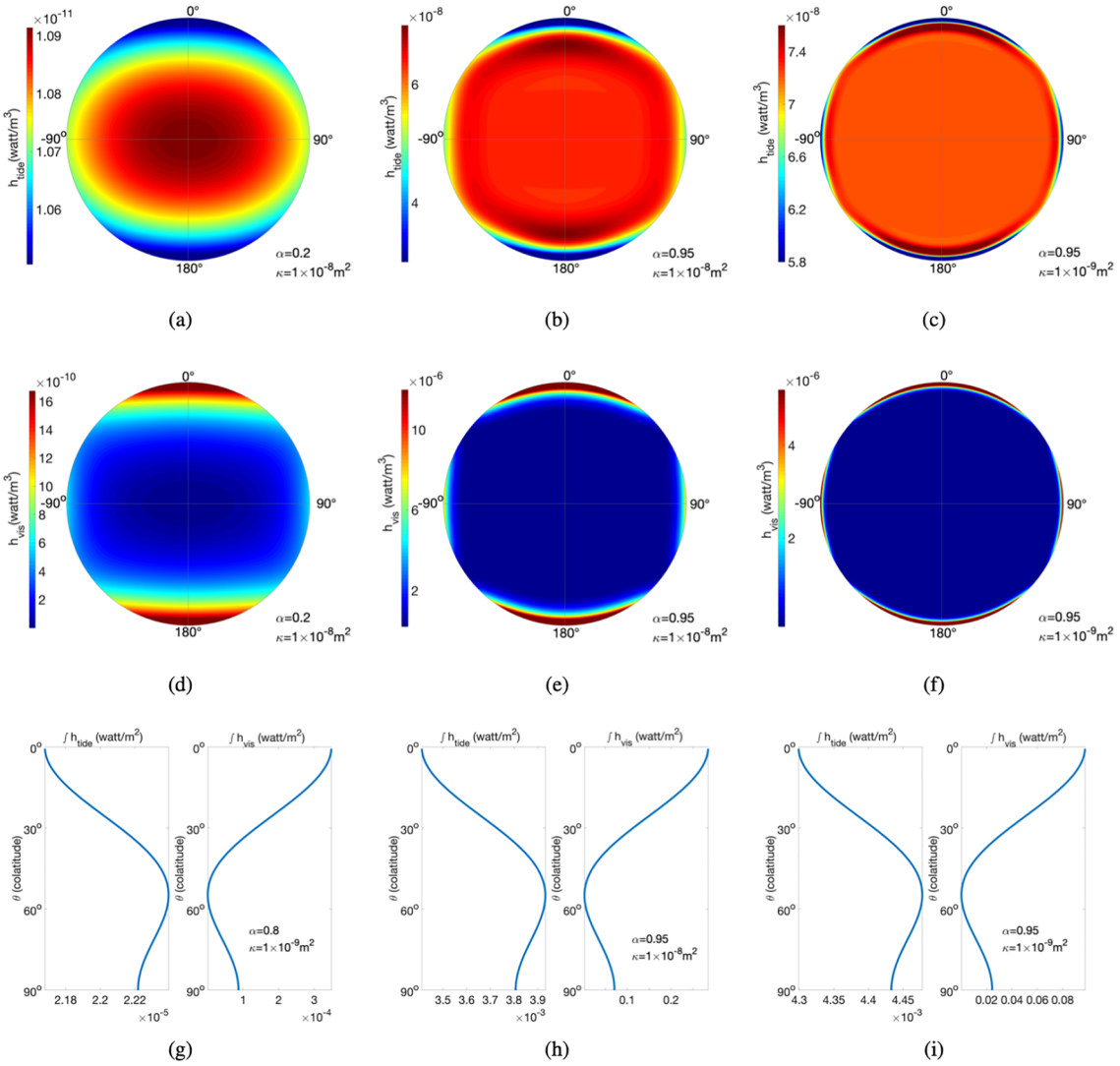

Figure 6. Distribution of volumetric tidal heating rates in solid matrix h_{tide} (a–c), viscous dissipation in pore fluid h_{vis} (d–f), and heat flux (radial integration of volumetric heating rates) for solid and fluid heating (g–i). The volumetric heating rates (a–f) are shown on a vertical cross section of the spherical body, and heat flux (g–i) is shown as functions of the colatitude. The heating rates are calculated assuming the simplified tidal potential with axisymmetric geometry. Panels (a), (d), and (g) correspond to permeability $\kappa = 10^{-8}$ m^2, poroelastic coefficient $\alpha = 0.2$; panels (b), (e), and (h) correspond to $\kappa = 10^{-9}$ m^2, $\alpha = 0.2$; panels (c), (f), and (i) correspond to $\kappa = 10^{-9}$ m^2,$\alpha = 0.8$. Other parameters including rock matrix rigidity $\mu = 1$ GPa and viscosity $\eta_m = 10^{17}$ Pa·s are assumed for all cases. The radius of the sphere is 186 km.

4. Evolution of Heating Rate With Weakening of the Core

The enhanced heating rates we find may also have implications for the thermal evolution in the history of Enceladus. As postulated by Choblet et al. (2017), cyclic deformation leads to progressive weakening of the core, which causes a reduction in viscosity and rigidity. It is therefore possible that the core of Enceladus possessed higher viscosity and rigidity in its past, which, according to the Maxwell model, corresponds to a negligible heating rate. But incorporation of a second phase (i.e., fluid) changes this conclusion, as follows.

Direct measurements of how viscosity and rigidity evolve over time due to periodic loading are not available. However, existing experimental studies provide relations for both the damping ratio D and effective modulus G, which are typical measurements in mechanical tests (Ishibashi & Zhang, 1993; Rollins et al., 1998; Seed et al., 1986). For Maxwell viscoelastic materials these quantities are determined by the

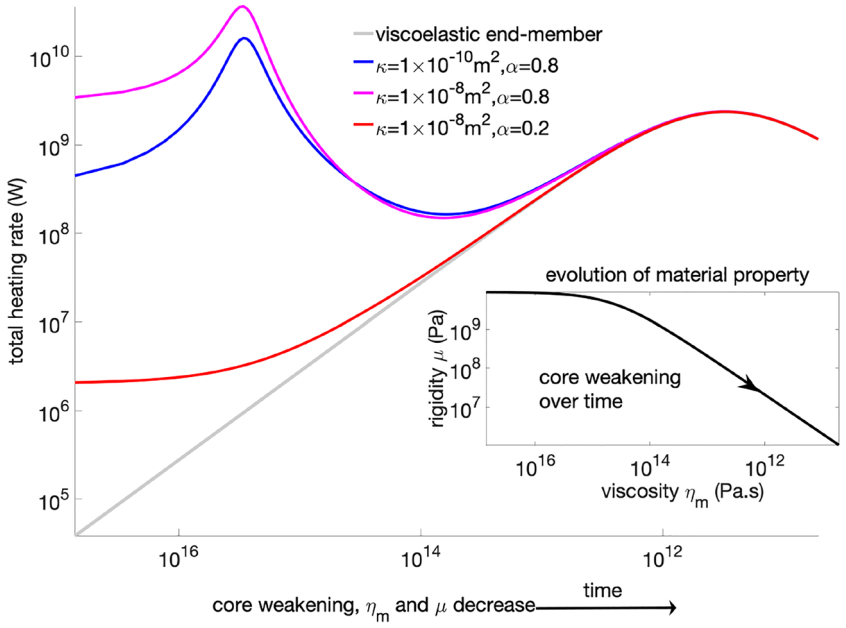

Figure 7. Possible heating trajectories during the weakening of the core. During the weakening, reduction of solid matrix viscosity and rigidity are approximated based on experimental data published in Rollins et al. (1998), as shown in the inset plot. The main horizontal axis shows decreasing viscosity, which indicates weakening over time. The classical tidal heating model would predict a monotonic increase of heating rate with time through most of the weakening trajectory (Choblet et al., 2017). For a two-phase core, there may exist a high heating period early in the moon's history, before sufficient weakening occurs.

complex rigidity μ^* as $D = Im(\mu^*)/2|\mu^*|$ and $G = |\mu^*|$ (Choblet et al., 2017), which further lead to the relations $\eta_m = \frac{G}{2D\omega}$, $\mu = \frac{G}{\sqrt{1-4D^2}}$. Here we infer a weakening trajectory based on the experimental data in (Rollins et al., 1998) on cyclically deformed gravels, where D and G are measured as functions of cyclic shear strain. Fitting a linear relation between D and G, we obtain from the experimental data the relation $D = -0.2086G/G_{\max} + 0.1828$ and choose a maximum effective modulus of $G_{\max} = 10$ GPa. During the weakening of the core, the effective modulus G decreases over time, leading to an increase in damping ratio D, and reduction in matrix viscosity η_m and rigidity μ (inset of Figure 7). According to viscoelastic tidal heating models, the heating rate increases as the core weakens (Choblet et al., 2017), and 10–30 GW of heat implies a severely weakened core with viscosity $\eta_m < 10^{13}$ Pa·s (Choblet et al., 2017). With the poroviscoelastic model, an enhanced heating rate is achievable at higher viscosity and rigidity (Figure 7), implying the possibility of intense heating in the early history of Enceladus, prior to severe weakening of its core. Prolonged heating in the deep past of Enceladus is certainly energetically possible, based on the rate at which energy can be supplied by Saturn (Nimmo et al., 2018). Furthermore, there are potentially interesting feedbacks, since early water-rock reactions could lead to alteration of the silicate mechanical properties (e.g., serpentinization) and a potential run-away effect.

5. Summary and Discussion

In this study we developed a poroviscoelastic description for the tidal heating process in the fluid-saturated core of an icy satellite and applied it to Enceladus. The poroviscoelastic rheology incorporates the coupling between the deformation of the solid rock matrix and fluid motion and requires reevaluation of the heat generated during tidal flexing in both the solid and fluid component of the core. Despite simplifications in loading geometry and boundary conditions, the new model is reasonably consistent with the classical viscoelastic models at its viscoelastic end-member state, reproducing the bulk part (57%) of the predicted total heating rate. When fluid-solid coupling effects are incorporated, the poroviscoelastic model predicts high heating rates, which can reach 10–30 GW without requiring the ultralow solid viscosities invoked by previous

work (Choblet et al., 2017; Efroimsky, 2018; Roberts, 2015). Based on the characteristics of these heating rates, we postulate that the heating rate enhancement results from both the compressibility of the solid matrix, and viscous dissipation of the fluid flows. The model also suggests that Enceladus may have undergone intense tidal heating early in its history, before the core was weakened. The volumetric fluid heating rate is maximized at shallow depths at the poles, and the surface heat flux from the fluid component peaks at the poles. Although our model provides a simplified description of the tidal deformation process, the enhanced heating rates suggest the importance of considering tidal heating problems in a two-phase framework where the fluid and solid components are kinematically coupled. To obtain more precise heating rates and distributions, future analytical work will need to incorporate an improved treatment of boundary conditions and the tidal forcing.

Our poroviscoelastic model also yields some results that are consistent with observations. The model predicts that the fluid heating (both volumetric heating rate and heat flux) likely concentrates in the polar regions, which could have possible implications for thickness variations of the ice shell of Enceladus and the high polar heat flux (Beuthe et al., 2016; Čadek et al., 2016; Hemingway & Mittal, 2019; Howett et al., 2011). The thinning of polar ice used to be primarily attributed to increased heating at the base of the ice shell near its melting point, while the effect of core heating was considered to be too small to be relevant (Běhounková et al., 2012; Tobie et al., 2008). Our model suggests that the local heating in the pore fluid and the resulting heat flux peak at polar surface regions. These high heating rates and heat flux could contribute to the thinning of polar ice shell.

There are several obvious ways in which this pilot study could be extended. One is to include a full treatment of the degree-2 tidal potential, rather than the axisymmetric potential assumed here. Doing so would allow a full exploration of the tidal forcing, and in particular help to provide a detailed constraint on the maximum strain in the polar regions. An intermediate step would be to focus on the effect of librations: the librational potential consists of a single degree-2 harmonic (e.g., Richard & Rambaux, 2014), and librations may have played an important role in Enceladus's evolution (Wisdom, 2004; Wilson & Kerswell, 2018). A second obvious improvement would be to use the heating derived to calculate the resulting thermal structure. This is not straightforward, however, because particularly in the high-permeability cases, the effects of fluid convection will need to be treated (cf. Choblet et al., 2017), likely in a parameterized fashion. But doing these calculations is important because it is not clear whether the permeabilities and heating rates assumed here are consistent with the high-temperature, water-rock reactions inferred by Hsu et al. (2015). Likewise, the periodic introduction of warm fluid into the base of the overlying ocean is likely to have important consequences for the ocean circulation above (cf. Vance et al., 2007) and the evolution of the ice shell thickness.

It is also of some interest to explore where else this analysis may be applied. Larger bodies with oceans and rocky cores, such as Europa, are likely to have a thinner permeable layer owing to the higher pressures. But the midsized Saturnian satellites, in particular Dione (which may have an ocean; Zannoni et al., 2020) are likely candidates for heating generate by a poroviscoelastic response to tidal forcing. A less obvious candidate is Io, which likely has a subsurface, partially molten permeable region in which tidal forcing is important (de Kleer et al., 2019). We conclude, in common with Choblet et al. (2017), that the core of Enceladus is likely a region of high heat production and fluid motion. Future work that studies the forces driving this heating and fluid motion in more detail will increase our capacity to evaluate the thermal evolution, the locations and likelihood or geochemistry and biochemistry below the sea floor of Enceladus.

Appendix A: Quantitative Details

A1. Solutions for Periodically Loaded Poroviscoelastic Body

During periodic deformation, interstitial pore water can flow through the porous and permeable solid matrix, driven by the gradient of pore pressure $P(r, \theta, t)$. Assuming a periodic form for all quantities $f(r, \theta, t) = Re\left[\hat{f}(r, \theta)e^{i\omega t}\right]$, Darcy's law and the continuity equation may be written as

Table A1
Ranges of Parameters Used in the Study

Symbol	Definition	Range of value/expression
R_o	core radius	186 km
α	poroelastic coefficient (Biot coefficient)	0–1
c	poroelastic diffusivity	$\frac{\kappa}{\eta_f}\frac{\left(K_m+\frac{4}{3}\mu_m\right)(K_u-K_m)}{\alpha^2\left(K_u+\frac{4}{3}\mu_m\right)}$
K_f	bulk modulus of pore water	2.2 GPa
K_s	bulk modulus of rock	10 GPa
ϕ_o	porosity of rock matrix	0.2
K_m	drained bulk modulus	$(1-\alpha)K_s$
K_u	undrained bulk modulus	$K_m+\frac{\alpha^2K_sK_f}{\phi_oK_s+(\alpha-\phi_o)K_f}$
μ	shear modulus (rigidity) of rock matrix	10^7–10^{10} Pa
η_f	pore water viscosity	0.0019 Pa·s
η_m	viscosity of the rock matrix	$10^{12}-10^{18}$ Pa·s
κ	permeability of rock matrix	10^{-11}–10^{-7} m^2
τ	viscoelastic relaxation time for rock matrix	η_m/μ
T_ω	orbital period	33 hr
ω	loading angular frequency	$\frac{2\pi}{T_\omega}$
δ	poroelastic skin depth	$\sqrt{c/\omega}$

$$\hat{\vec{q}}+\frac{\kappa}{\eta_f}\nabla\hat{P}=0, \tag{A1}$$

$$i\omega\hat{\zeta}+\nabla\cdot\hat{\vec{q}}=0. \tag{A2}$$

Here $\hat{\vec{q}}$ is complex Darcy's velocity, κ is the permeability of the rock matrix, η_f is the viscosity of the pore water. The variation in fluid content $\zeta(r,\theta,t)$ is defined as the volume of pore fluid entering or leaving the pore space for a unit undeformed volume (Biot, 1941; Cheng, 2016). The stress-strain relation for a poroviscoelastic material can be expressed in complex form similar to linear poroelasticity,

$$\hat{\sigma}=\left(K_m-\frac{2}{3}\mu^*\right)Tr(\hat{\epsilon})I+2\mu^*\hat{\epsilon}-\alpha\hat{P}I, \tag{A3}$$

where α is the poroelastic coefficient (also known as the Biot constant) ranging from 0 to 1 and is constructed via micromechanical relation $\alpha=1-K_m/K_s$ (Cheng, 2016; Rice & Cleary, 1976). When $\alpha=0$ the constitutive relation reduces to the Maxwell formulation in classical tidal heating studies (Brusche & Sundermann, 1978; Peale & Cassen, 1978; Ross & Schubert, 1989; Segatz et al., 1988; Tobie et al., 2005; Wu & Peltier, 1982). The complex rigidity μ^* is defined as

$$\mu^*=\mu\frac{i\omega\tau}{1+i\omega\tau}, \tag{A4}$$

where $\tau=\eta_m/\mu$ is the viscoelastic relaxation time. An irrotational displacement is assumed to arise from an axisymmetric degree-2 displacement potential $\hat{\vec{u}}=\nabla\hat{\Phi}$ (Landau & Lifshitz, 1959; Love, 1927), and volumetric deformation becomes $Tr(\hat{\epsilon})=\nabla^2\hat{\Phi}$. In addition to the stress-strain relation, the poroelastic constitutive relations also prescribe a linear relationship between pore pressure P and fluid content ζ, which is independent of the viscoelastic relaxation (Biot, 1941; Cheng, 2016; Rice & Cleary, 1976),

$$\hat{\zeta}=\alpha\left(\nabla^2\hat{\Phi}+\frac{\alpha}{K_u-K_m}\hat{P}\right) \tag{A5}$$

where the undrained modulus K_u is the bulk modulus of the rock-fluid ensemble (see Table A1). Since we simplify the geometry of the problem in the model, we do not explicitly account for the tidally varying gravitational potential (which involves all three degree-2 geometries) in the forcing equation. Instead, we simply assume a quasi-static equilibrium condition $\nabla\cdot\hat{\sigma}=0$ here and enforce the tidal forcing through the surface condition as described below. By choosing solutions with axisymmetric degree-2 pattern and periodicity, the axisymmetric part of the gravitational potential is implicitly accounted for (see below). The constitutive relations (A1, A2-1, and A5) and the quasi-equilibrium condition lead to

$$\nabla^2\hat{P}+k^2\hat{P}=0, \tag{A6}$$

with a complex wavenumber

$$k=\frac{1-i}{\sqrt{2}}\sqrt{\frac{\omega}{c}}\sqrt{\frac{K_u^o+i\omega\tau}{K_m^o+i\omega\tau}},$$

where material constants K_m^o, K_u^o and poroelastic diffusivity c are

$$K^o_{m,u} = \frac{K_{m,u}}{\left(K_{m,u} + \frac{4}{3}\mu\right)}, \quad c = \frac{\kappa}{\eta_f}\frac{\left(K_m + \frac{4}{3}\mu\right)(K_u - K_m)}{\left(K_u + \frac{4}{3}\mu\right)\alpha^2}.$$

When the rock matrix is deformable but incompressible, the pore fluid does not share the load of the system ($\alpha = 0, K_s = \infty$), and the evolution of the pore fluid pressure reduces to the Navier equation for porous flows in an incompressible matrix, which is typically assumed in hydrothermal circulation studies, for example (Choblet et al., 2017; Fisher et al., 2003). The general form of solution for Equation A6 in spherical coordinates, with an implicit boundary condition that the solution is finite at $r = 0$, is

$$\hat{P} = \sum_l \sum_{m \in [-l,\ l]} C_{l,m} j_l(kr) P_l^m(\cos\theta) e^{im\varphi},$$

where $j_l(kr)$ is an degree-l spherical Bessel function, P_l^m is degree-l associated Legendre polynomial, and $C_{l,m}$ are coefficients to be determined by initial and boundary conditions. With the axisymmetric condition ($m = 0$) and imposed degree-2 symmetry ($l = 2$), the solution reduces to

$$\hat{P} = C_1(3\cos 2\theta + 1)\left(3\frac{\sin kr}{k^3r^3} - 3\frac{\cos kr}{k^2r^2} - \frac{\sin kr}{kr}\right). \tag{A7}$$

Substituting Equation A7 into the equilibrium condition $\nabla^2\hat{\Phi} = \frac{\alpha}{\left(K_m + \frac{4}{3}\mu^*\right)}\hat{P}$ leads to the solution for the displacement potential

$$\hat{\Phi} = -\frac{\alpha C_1}{k^2\left(K_m + \frac{4}{3}\mu^*\right)} j_2(kr)(3\cos 2\theta + 1) + C_2 r^2(3\cos 2\theta + 1), \tag{A8}$$

where the second term is a general solution to the Laplace equation in viscoelastic heating problem (Kaula, 1964; Segatz et al., 1988; Tobie et al., 2005; Wu & Peltier, 1982). Under the constitutive relations, Equations A7 and A8 lead to solutions for other quantities,

$$\begin{aligned}
\hat{\epsilon_{rr}} &= \frac{\partial^2\hat{\Phi}}{\partial r^2}, & \hat{\sigma_{rr}} &= \left(K_m - \frac{2}{3}\mu^*\right)\nabla^2\hat{\Phi} + 2\mu^*\hat{\epsilon_{rr}} - \alpha\hat{P},\\
\hat{\epsilon_{\theta\theta}} &= \frac{1}{r^2}\frac{\partial^2\hat{\Phi}}{\partial\theta^2} + \frac{1}{r}\frac{\partial\hat{\Phi}}{\partial r}, & \hat{\sigma_{\theta\theta}} &= \left(K_m - \frac{2}{3}\mu^*\right)\nabla^2\hat{\Phi} + 2\mu^*\hat{\epsilon_{\theta\theta}} - \alpha\hat{P},\\
\hat{\epsilon_{\varphi\varphi}} &= \frac{1}{r}\frac{\partial\hat{\Phi}}{\partial r} + \frac{\cos\theta}{r^2\sin\theta}\frac{\partial\hat{\Phi}}{\partial\theta}, & \hat{\sigma_{\varphi\varphi}} &= \left(K_m - \frac{2}{3}\mu^*\right)\nabla^2\hat{\Phi} + 2\mu^*\hat{\epsilon_{\phi\phi}} - \alpha\hat{P},\\
\hat{\epsilon_{r\theta}} &= \frac{1}{2}\frac{\partial}{\partial r}\left(\frac{1}{r}\frac{\partial\hat{\Phi}}{\partial\theta}\right) - \frac{1}{2r^2}\frac{\partial\hat{\Phi}}{\partial\theta} + \frac{1}{2r}\frac{\partial^2\hat{\Phi}}{\partial\theta\partial r}, & \hat{\sigma_{r\theta}} &= 2\mu^*\hat{\epsilon_{r\theta}},\\
\hat{q_r} &= -\frac{\kappa C_1}{\eta_f}(3\cos 2\theta + 1)\frac{dj_2(kr)}{dr}, & & \\
\hat{q_\theta} &= 6\frac{\kappa C_1}{\eta_f}\sin\ 2\theta\ \frac{j_2(kr)}{r}, & & \\
\hat{\zeta} &= C_1\frac{\alpha^2\left(K_u + \frac{4}{3}\mu^*\right)}{\left(K_m + \frac{4}{3}\mu^*\right)(K_u - K_m)}(3\cos 2\theta + 1)j_2(kr), & &
\end{aligned} \tag{A9}$$

where $\hat{q_r}$ and $\hat{q_\theta}$ are complex amplitudes for the radial and tangential components of the Darcy's velocity. The solutions (A7–A9) contain two complex constants C_1,C_2, which are constrained by the following

boundary conditions. We specify continuity of fluid pressure and force balance at the surface of the core (Liao et al., 2018)

$$\sigma_{rr}(R_0, \theta) = -P_{ocean}(\theta), \quad P(R_0, \theta) = P_{ocean}(\theta),$$

where $\sigma_{rr}(R_0, \theta)$ is the radial component of the total stress in the core at the surface. $P_{ocean}(\theta)$ is the fluid pressure applied by the overlying ocean at the seafloor. Without specifying the ocean's pressure, we use the above two relationships to derive the fluid-loading condition $\hat{P}(R_0, \theta)+\hat{\sigma_{rr}}(R_0, \theta) = 0$, which leads to

$$C_2 = C_1\left[\frac{1}{2}\frac{\alpha}{k^2\left(K_m+\frac{4}{3}\mu^*\right)}\frac{d^2j_2}{dr^2}(kR_0)+\frac{1}{2}\frac{\alpha}{K_m+\frac{4}{3}\mu^*}j_2(kR_0)-\frac{1}{4\mu^*}j_2(kR_0)\right].$$

To constrain C_1, an additional boundary condition on the maximum strain at the poles is assumed. For diurnal tides the maximum tidal strain $\epsilon_{max} \approx 3e\frac{M}{m}\frac{R_0^3}{a^3}h_2$, where e is eccentricity of the orbit, M and m are the mass of the planet and moon, R_0 is the radius of the moon, and a the planet-satellite distance; $h_2 = \frac{5}{3}k_2$ is the tidal rising Love number (Murray & Dermott, 1999). Following Kepler's law the relationship may be written as $\epsilon_{max} = \frac{9}{4\pi}e\frac{\omega^2}{\rho G}\frac{5}{3}k_2$, $k_2 = \frac{3}{5}\frac{3/2}{1+19\mu^*/2\rho gR}$. We assume that at the pole of the core the magnitude reaches the maximum value $\epsilon_0 = \frac{9}{4\pi}e\frac{\omega^2}{\rho G}\frac{5}{3}|k_2|$. For each set of η_m and μ, the boundary condition $\hat{\epsilon_{rr}}(R_0, 0^o) = \epsilon_0$ is used for constraining C_1 via equation A8.

The volumetric heating rates h_{tide} and h_{vis} are obtained by (Al-Hadhrami et al., 2003; Cheng, 2016; Segatz et al., 1988; Tobie et al., 2005)

$$h_{tide} = \Sigma_{i,j}\frac{1}{T_\omega}\int_{nT_\omega}^{(n+1)T_\omega}\sigma_{ij}\frac{\partial\epsilon_{ij}}{\partial t}dt+\frac{1}{T_\omega}\int_{nT_\omega}^{(n+1)T_\omega}P_f\frac{\partial\zeta}{\partial t}dt,\ h_{vis} = \frac{1}{T_\omega}\int_{nT_\omega}^{(n+1)T_\omega}\frac{\eta_f}{\kappa}\vec{q}\cdot\vec{q}\,dt, \tag{A10}$$

where $\Sigma_{i,j}$ indicates summation of all the indices. Substituting complex formulations into Equation A10 leads to

$$h_{tide} = -\frac{\omega}{2}\Sigma_{ij}\left[Re(\hat{\sigma_{ij}})Im(\hat{\epsilon_{ij}})-Im(\hat{\sigma_{ij}})Re(\hat{\epsilon_{ij}})\right]-\frac{\omega}{2}\left[Re(\hat{P_f})Im(\hat{m})-Im(\hat{P_f})Re(\hat{m})\right],\ h_{vis} = \frac{1}{2}\frac{\eta_f}{\kappa}(|\hat{q}_r|^2+|\hat{q}_\theta|^2), \tag{A11}$$

and the total heating rate is calculated by volume integration of each heating rate

$$H_{tide,\,vis} = 2\pi\int_0^{R_0}\int_0^{\pi}h_{tide,\,vis}(r, \theta)r^2\sin\theta d\theta dr.$$

A2. End-Member Case: Tidal Heating of an Effectively Viscoelastic Body

The poroviscoelastic body behaves effectively as a purely viscoelastic one if the pore pressure is decoupled from the loading of the solid matrix ($\alpha = 0$), or when the pore fluid is unable to flow (e.g., $\kappa = 0$). In these cases, the strain-stress relation becomes identical to that of a viscoelastic body (Roberts & Nimmo, 2008; Ross & Schubert, 1989; Tobie et al., 2005)

$$\hat{\sigma}_{visco} = \left(K-\frac{2}{3}\mu^*\right)\nabla^2\hat{\Phi}_{visco}I+2\mu^*\hat{\epsilon}_{visco}, \tag{A12}$$

where K is the bulk modulus ($K = K_m$ if the system is drained or $K = K_u$ if the system is undrained). The quasi-equilibrium condition $\nabla\cdot\sigma = 0$ leads to the Laplace equation for potential $\hat{\Phi}_{visco}$ and a solution with degree-2 symmetry,

$$\nabla^2\hat{\Phi}_{visco} = 0 \quad \rightarrow \quad \hat{\Phi}_{visco} = C_3 r^2(3\cos 2\theta + 1), \tag{A13}$$

which reduces the strain-stress relation to

$$\hat{\sigma}_{visco} = 2\mu^*\hat{\epsilon}_{visco},$$

and leads to heating rate

$$h_{visco} = \frac{1}{T_\omega}\int_{nT_\omega}^{(n+1)T_\omega} dt\Sigma Re(\sigma_{ij}) Re\left(\frac{\partial \epsilon_{ij}}{\partial t}\right) = \frac{\omega}{2} Im(2\mu^*)\Sigma|\hat{\epsilon}_{ij}|^2 = 96C_3^2\omega Im(\mu^*), \tag{A14}$$

where C_3 is to be determined by the same maximum strain boundary condition. The heating rate h_{visco} is uniform in space because of the simplified form of Equation A13 arising from the implicit condition $\Phi_{visco}|_{r\to 0} \neq \infty$.

Appendix B: Additional Results

Figures B1–B4 show the volumetric heating rates as functions of viscosity η_m, the ratio between viscous dissipation in fluid and tidal heating in solid as a function of the viscosity η_m, Biot constant α and permeability κ, the maximal tidal fluid responses, and the tidal and viscous heating in a shallow crust, respectively.

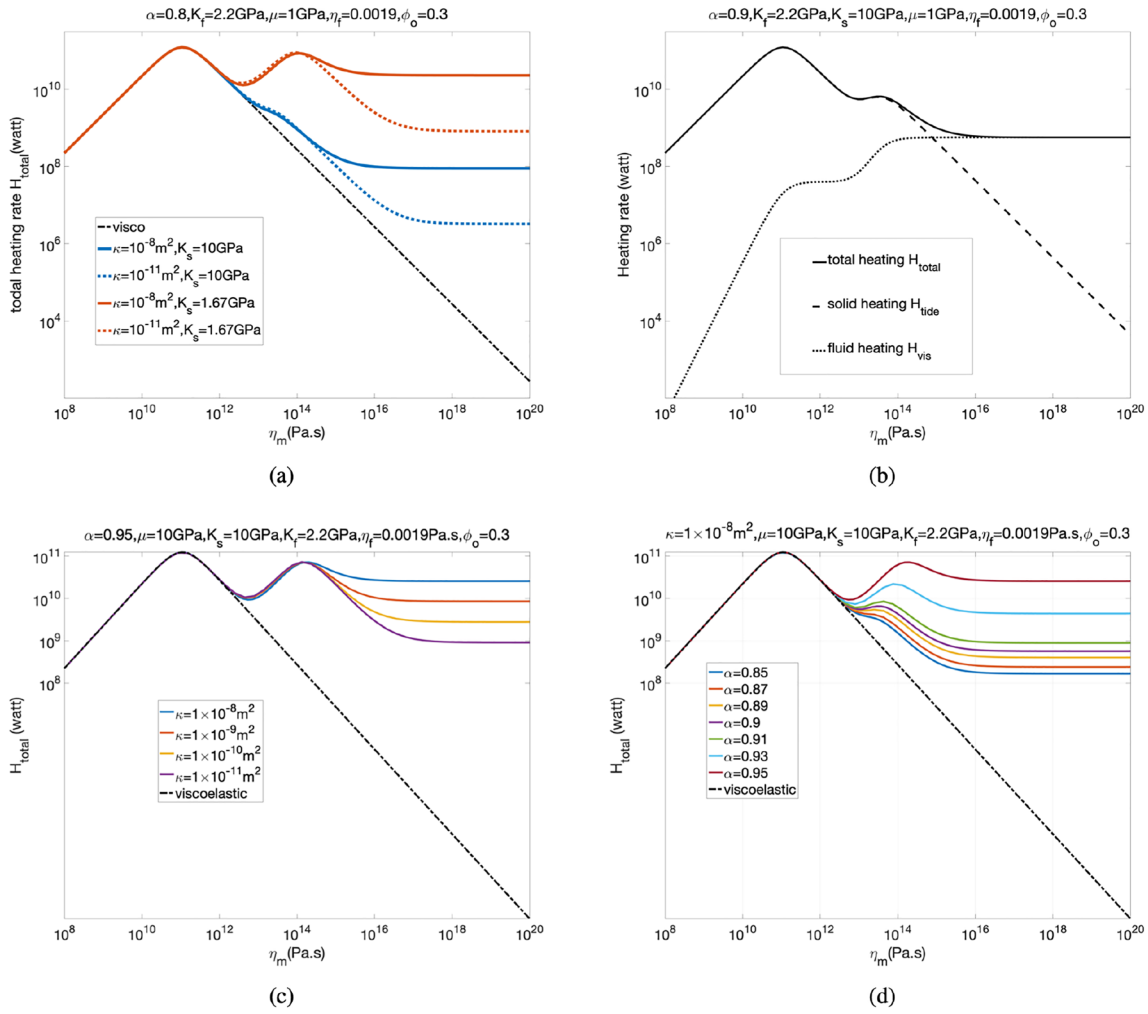

Figure B1. (a) Total heating rate for different solid bulk modulus K_s. A second heating peak appears when K_s is small, indicating that the enhanced heating is linked to increased compressibility of the rock matrix. (b) Total heating rate, solid heating rate, and fluid heating rate as functions of solid viscosity for one set of parameters. (c) Total heating rates for different α values and (d) total heating rates for different permeability values. Panels (c) and (d) indicate that the second heating rate peak migrates to higher viscosity for larger α but does not depend on permeability.

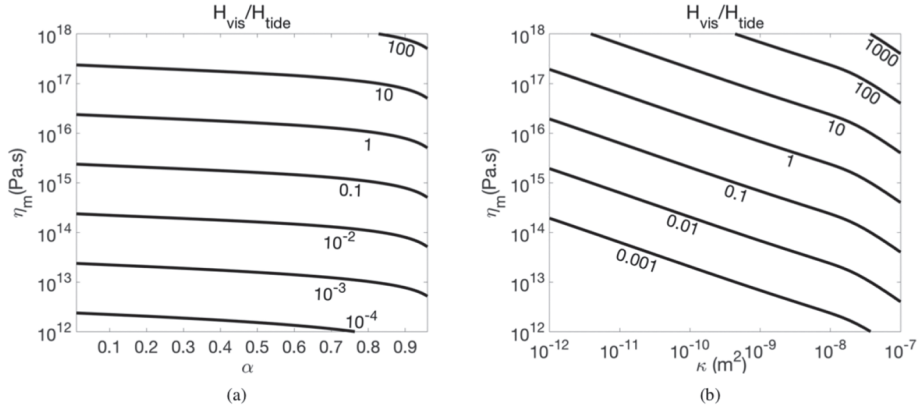

Figure B2. Contours of ratio between heating in pore fluid and solid matrix H_{vis}/H_{tide} varying with pairs of parameters. For panel (a), permeability $\kappa = 1 \times 10^{-10}$ m^2; for panel (b), poroelastic coefficient $\alpha = 0.2$. The dependence of H_{vis}/H_{tide} on rigidity μ is negligible and hence is not shown.

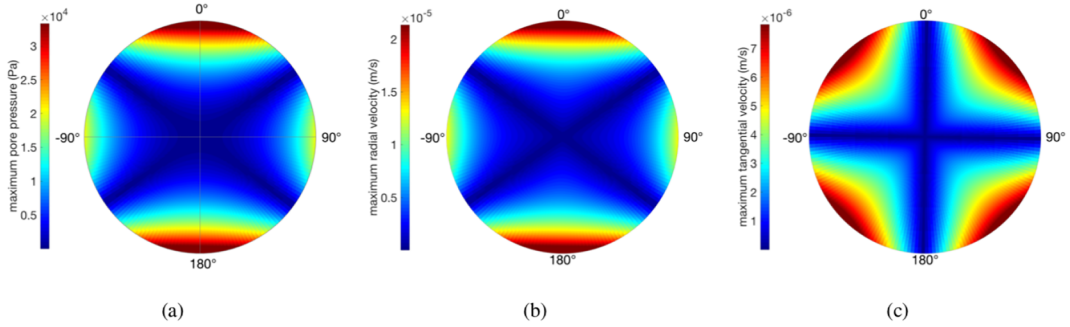

Figure B3. Maximum pore pressure $|\hat{P}|$, radial component $|\hat{q}_r|$, and tangential component $|\hat{q}_\theta|$ of Darcy's velocity. The solutions are obtained based on maximum strain condition, viscosity $\eta_m = 10^{16}$ Pa·s, rigidity $\mu = 1$ GPa, $\alpha = 0.1$, $\kappa = 10^{-8}$ m^2, $\phi_o = 20\%$. Globally averaged radial fluid velocity is $< |\hat{q}_r|/\phi_o > \; = 3.79 \times 10^{-6}$ m/s and tangential velocity is $< |\hat{q}_\theta|/\phi_o > \; = 2.20 \times 10^{-6}$ m/s.

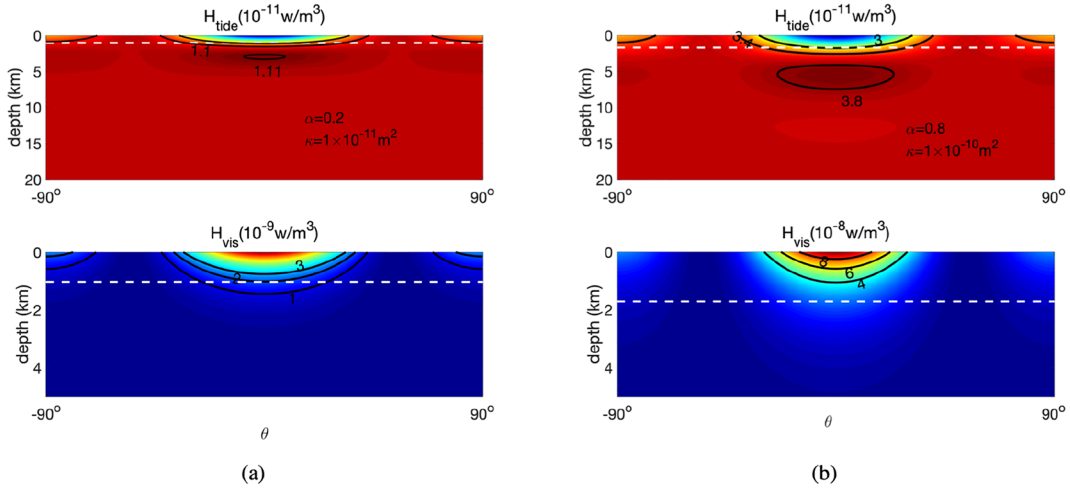

Figure B4. Examples of volumetric heating rate and contours in shallow crust in a hemisphere for two different parameter combinations κ and α combination. For both cases $\eta_m = 10^{17}$ Pa·s, $\mu = 1$GPa, and $\phi_o = 0.2$. White dash lines indicate the skin depth $\delta = \sqrt{c/\omega}$ for oscillating poroelastic material (Jupp & Schultz, 2004). The horizontal axis shows colatitude θ, where $\theta = 0$ indicates polar region.

Data Availability Statement

Matlab codes for realizing the analytical solutions are available at Code Ocean (Liao, 2020).

Acknowledgments
We thank David Bercovici and Peter Driscoll for helpful discussions and input to the model. We thank two reviewers, Gabriel Tobie and Michael Efroimsky, and Editor Laurent Montesi for reviewing the manuscript.

References

Al-Hadhrami, A. K., Elliott, L., & Ingham, D. B. (2003). A new model for viscous dissipation in porous media across a range of permeability values. *Transport in Porous Media*, *53*(1), 117–122. https://doi.org/10.1023/A:1023557332542

Běhounková, M., Tobie, G., Choblet, G., & Čadek, O. (2012). Tidally-induced melting events as the origin of south-pole activity on Enceladus. *Icarus*, *219*(2), 655–664. https://doi.org/10.1016/j.icarus.2012.03.024

Beuthe, M. (2013). Spatial patterns of tidal heating. *Icarus*, *223*(1), 308–329. https://doi.org/10.1016/j.icarus.2012.11.020

Beuthe, M., Rivoldini, A., & Trinh, A. (2016). Enceladus's and Dione's floating ice shells supported by minimum stress isostasy. *Geophysical Research Letters*, *43*, 10,088–10,096. https://doi.org/10.1002/2016GL070650

Biot, M. A. (1941). General theory of three-dimensional consolidation. *Journal of Applied Physics*, *12*, 155.

Brusche, P., & Sundermann, J. (1978). *Tidal friction and the Earth's rotation*. New York: Springer-Verlag Berlin Heidelberg.

Čadek, O., Tobie, G., Van Hoolst, T., Massé, M., Choblet, G., Lefèvre, A., et al. (2016). Enceladus's internal ocean and ice shell constrained from Cassini gravity, shape, and libration data. *Geophysical Research Letters*, *43*, 5653–5660. https://doi.org/10.1002/2016GL068634

Chen, E. M. A., & Nimmo, F. (2011). Obliquity tides do not significantly heat Enceladus. *Icarus*, *214*(2), 779–781.

Cheng, A. H.-D. (2016). *Poroelasticity*. Cham, Switzerland: Springer International. https://doi.org/10.1007/978-3-319-25202-5

Choblet, G., Tobie, G., Sotin, C., Běhounková, M., Čadek, O., Postberg, F., & Souček, O. (2017). Powering prolonged hydrothermal activity inside Enceladus. *Nature Astronomy*, *1*(12), 841–847. https://doi.org/10.1038/s41550-017-0289-8

Crone, T., & Wilcock, W. (2005). Modeling the effects of tidal loading on mid-ocean ridge hydrothermal systems. *Geochemistry, Geophysics, Geosystems*, *6*, Q07001. https://doi.org/10.1029/2004GC000905

de Kleer, K., Park, R., & McEwen, A. S. (2019). Tidal heating: Lessons from Io and the Jovian System-Final report: Keck Institute for Space Studies.

Efroimsky, M. (2018). Tidal viscosity of Enceladus. *Icarus*, *300*, 223–226. https://doi.org/10.1016/j.icarus.2017.09.013

Fisher, A. T., Davis, E. E., Hutnak, M., Spiess, V., Zühlsdorff, L., Cherkaoui, A., et al. (2003). Hydrothermal recharge and discharge across 50 km guided by seamounts on a Young Ridge Flank. *Nature*, *421*(6923), 618.

Hay, H. C. F. C., & Matsuyama, I. (2017). Numerically modelling tidal dissipation with bottom drag in the oceans of Titan and Enceladus. *Icarus*, *281*, 342–356.

Hemingway, D. J., Iess, L., Tajeddine, R., & Tobie, G. (2018). The interior of Enceladus. In *Enceladus and the icy moons of Saturn* (Vol. 1, pp. 57–77). University of Arizona Press.

Hemingway, D. J., & Mittal, T. (2019). Enceladus's ice shell structure as a window on internal heat production. *Enceladus's Ice Shell Structure as a Window on Internal Heat Production*, *332*, 111–131. https://doi.org/10.1016/j.icarus.2019.03.011

Howett, C. J. A., Spencer, J. R., Pearl, J., & Segura, M. (2011). High heat flow from Enceladus' south polar region measured using 10–600 cm 1 Cassini/CIR S data. *Journal of Geophysical Research*, *116*, E03003. https://doi.org/10.1029/2010JE003718

Hsu, H.-W., Postberg, F., Sekine, Y., Shibuya, T., Kempf, S., Horányi, M., et al. (2015). Ongoing hydrothermal activities within Enceladus. *Nature*, *519*, 207. https://doi.org/10.1038/nature14262

Hurford, T. A., Frey, S., & Greenberg, R. (2006). Numerical evaluation of Love's solution for tidal amplitude. In B. A. Steves, A. J. Maciejewski, M. Hendry (Eds.), *Chaotic worlds: From order to disorder in gravitational N-body dynamical systems* (pp. 307–323). Dordrecht: Springer Netherlands.

Iess, L., Stevenson, D. J., Parisi, M., Hemingway, D. J., Jacobson, R. A., Lunine, J. I., et al. (2014). The gravity field and interior structure of Enceladus. *Science*, *344*(6179), 78–80.

Ishibashi, I., & Zhang, X. (1993). Unified dynamic shear moduli and damping ratios of sand and clay. *Soils and Foundations*, *33*(1), 182–191.

Jupp, T. E., & Schultz, A. (2004). A poroelastic model for the tidal modulation of seafloor hydrothermal systems. *Journal of Geophysical Research*, *109*(B3), B03105. https://doi.org/10.1029/2003JB002583

Kaula, W. M. (1964). Tidal dissipation by solid friction and the resulting orbital evolution. *Reviews of Geophysics*, *2*(4), 661–685. https://doi.org/10.1029/RG002i004p00661

Kelley, D. S., Karson, J. A., Früh-Green, G. L., Yoerger, D. R., Shank, T. M., Butterfield, D. A., et al. (2005). A serpentinite-hosted ecosystem: The lost city hydrothermal field. *Science*, *307*(5714), 1428–1434.

Kite, E. S., & Rubin, A. M. (2016). Sustained eruptions on Enceladus explained by turbulent dissipation in tiger stripes. *Proceedings of the National Academy of Sciences*, *113*(15), 3972–3975.

Landau, L. D., & Lifshitz, E. M. (1959). *Theory of elasticity*. Oxford, UK: Pergamon Press.

Lauer, R. M., Fisher, A. T., & Winslow, D. M. (2018). Three-dimensional models of hydrothermal circulation through a seamount network on fast-spreading crust. *Earth and Planetary Science Letters*, *501*, 138–151. https://doi.org/10.1016/j.epsl.2018.08.025

Lemasquerier, D., Grannan, A. M., Vidal, J., Cébron, D., Favier, B., Le Bars, M., & Aurnou, J. M. (2017). Libration-driven flows in ellipsoidal shells. *Journal of Geophysical Research: Planets*, *122*, 1926–1950. https://doi.org/10.1002/2017JE005340

Liao, Y. (2020). Poroviscoelastic tidal heating. https://www.codeocean.com/. https://doi.org/10.24433/CO.8645626.v1

Liao, Y., Soule, A., & Jones, M. (2018). On the mechanical effects of poroelastic crystal mush in classical magma chamber models. *Journal of Geophysical Research: Solid Earth*, *123*, 9376–9406. https://doi.org/10.1029/2018JB015985

Love, A. (1927). *A treatise on the theory mathematical of elasticity*. Cambridge, UK: Cambridge University Press.

Matsuyama, I., Beuthe, M., Hay, H. C. F. C., Nimmo, F., & Kamata, S. (2018). Ocean tidal heating in icy satellites with solid shells. *Icarus*, *312*, 208–230.

Mayhew, L. E., Ellison, E. T., McCollom, T. M., Trainor, T. P., & Templeton, A. S. (2013). Hydrogen generation from low-temperature water–rock reactions. *Nature Geoscience*, *6*, 478. https://doi.org/10.1038/ngeo1825

Murray, C. D., & Dermott, S. F. (1999). *Solar system dynamics*. Cambridge, UK: Cambridge University Press.

Neveu, M., & Rhoden, A. R. (2019). Evolution of Saturn's mid-sized moons. *Nature Astronomy*, *3*(6), 543–552. https://doi.org/10.1038/s41550-019-0726-y

Nimmo, F., Barr, A. C., Běhounková, M., & McKinnon, W. B. (2018). The thermal and orbital evolution of Enceladus: Observational constraints and models. *Enceladus and the Icy Moons of Saturn*, 79–88.

Peale, S. J., & Cassen, P. (1978). Contribution of tidal dissipation to lunar thermal history. *Icarus*, *36*(2), 245–269. https://doi.org/10.1016/0019-1035(78)90109-4
Porco, C. C., Helfenstein, P., Thomas, P. C., Ingersoll, A. P., Wisdom, J., West, R., et al. (2006). Cassini observes the active south pole of Enceladus. *Science*, *311*(5766), 1393–1401.
Postberg, F., Kempf, S., Schmidt, J., Brilliantov, N., Beinsen, A., Abel, B., et al. (2009). Sodium salts in *e*-ring ice grains from an ocean below the surface of Enceladus. *Nature*, *459*(7250), 1476–4687.
Postberg, F., Khawaja, N., Abel, B., Choblet, G., Glein, C. R., Gudipati, M. S., et al. (2018). Macromolecular organic compounds from the depths of Enceladus. *Nature*, *558*(7711), 564–568. https://doi.org/10.1038/s41586-018-0246-4
Postberg, F., Schmidt, J., Hillier, J., Kempf, S., & Srama, R. (2011). A salt-water reservoir as the source of a compositionally stratified plume on Enceladus. *Nature*, *474*(7353).
Rice, J. R., & Cleary, M. P. (1976). Some basic stress diffusion solutions for fluid-saturated elastic porous media with compressible constituents. *Reviews of Geophysics*, *14*(2), 227–241. https://doi.org/10.1029/RG014i002p00227
Richard, A., & Rambaux, N. (2014). Complements to the longitudinal librations of an elastic 3-layer titan on a non-Keplerian orbit. *Proceedings of the International Astronomical Union*, *9*(S310), 21–24.
Roberts, J. H. (2015). The fluffy core of Enceladus. *Icarus*, *258*, 54–66. https://doi.org/10.1016/j.icarus.2015.05.033
Roberts, J. H., & Nimmo, F. (2008). Tidal heating and the long-term stability of a subsurface ocean on Enceladus. *Icarus*, *194*(2), 675–689.
Rollins, K. M., Evans, M. D., Diehl, N. B., & Daily, W. D. III (1998). Shear modulus and damping relationships for gravels. *Journal of Geotechnical and Geoenvironmental Engineering*, *124*(5), 396–405.
Ross, M. N., & Schubert, G. (1989). Viscoelastic models of tidal heating in Enceladus. *Icarus*, *78*(1), 90–101. https://doi.org/10.1016/0019 - 1035(89)90071-7
Russell, M. J., Hall, A. J., & Martin, W. (2010). Serpentinization as a source of energy at the origin of life. *Geobiology*, *8*(5), 355–371.
Schrenk, M. O., Brazelton, W. J., & Lang, S. Q. (2013). Serpentinization, carbon, and deep life. *Reviews in Mineralogy and Geochemistry*, *75*(1), 575–606.
Schwarzenbach, E. M. (2016). Serpentinization and the formation of fluid pathways. *Geology*, *44*(2), 175–176.
Seed, H. B., Wong, R. T., Idriss, I. M., & Tokimatsu, K. (1986). Moduli and damping factors for dynamic analyses of cohesionless soils. *Journal of Geotechnical Engineering*, *112*(11), 1016–1032.
Segatz, M., Spohn, T., Ross, M. N., & Schubert, G. (1988). Tidal dissipation, surface heat flow, and figure of viscoelastic models of Io. *Icarus*, *75*(2), 187–206. https://doi.org/10.1016/0019-1035(88)90001-2
Sekine, Y., Shibuya, T., Postberg, F., Hsu, H.-W., Suzuki, K., Masaki, Y., et al. (2015). High-temperature water–rock interactions and hydrothermal environments in the chondrite-like core of Enceladus. *Nature Communications*, *6*, 8604. https://doi.org/10.1038/ncomms9604
Shoji, D., Hussmann, H., Kurita, K., & Sohl, F. (2013). Ice rheology and tidal heating of Enceladus. *Icarus*, *226*(1), 10–19.
Souček, O., Běhounková, M., Čadek, O., Hron, J., Tobie, G., & Choblet, G. (2019). Tidal dissipation in Enceladus' uneven, fractured ice shell. *Icarus*, *328*, 218–231.
Taubner, R.-S., Leitner, J. J., Firneis, M. G., & Hitzenberger, R. (2015). Modelling the interior structure of Enceladus based on the 2014's Cassini gravity data. *Origins of Life and Evolution of Biospheres*, *46*(2), 283–288. https://doi.org/10.1007/s11084-015-9475-9
Thomas, P. C., Tajeddine, R., Tiscareno, M. S., Burns, J. A., Joseph, J., Loredo, T. J., et al. (2016). Enceladus's measured physical libration requires a global subsurface ocean. *Icarus*, *264*, 37–47. https://doi.org/10.1016/j.icarus.2015.08.037
Tobie, G., Mocquet, A., & Sotin, C. (2005). Tidal dissipation within large icy satellites: Applications to Europa and Titan. *Icarus*, *177*(2), 534–549.
Tobie, G., Čadek, O., & Sotin, C. (2008). Solid tidal friction above a liquid water reservoir as the origin of the south pole hotspot on Enceladus. *Icarus*, *196*(2), 642–652. https://doi.org/10.1016/j.icarus.2008.03.008
Travis, B. J., & Schubert, G. (2014). Keeping Enceladus warm. *Icarus*, *250*, 32–42. https://doi.org/10.1016/j.icarus.2014.11.017
Tyler, R. H. (2009). Ocean tides heat Enceladus. *Geophysical Research Letters*, *36*, L15205. https://doi.org/10.1029/2009GL038300
Vance, S., Harnmeijer, J., Kimura, J., Hussmann, H., DeMartin, B., & Brown, J. M. (2007). Hydrothermal systems in small ocean planets. *Astrobiology*, *7*(6), 987–1005.
Vance, S., Panning, M. P., Stähler, S., Cammarano, F., Bills, B. G., Tobie, G., et al. (2018). Geophysical investigations of habitability in ice-covered ocean worlds. *Journal of Geophysical Research: Planets*, *123*, 180–205. https://doi.org/10.1002/2017JE005341
Waite, J. H., Glein, C. R., Perryman, R. S., Teolis, B. D., Magee, B. A., Miller, G., et al. (2017). Cassini finds molecular hydrogen in the Enceladus plume: Evidence for hydrothermal processes. *Science*, *356*(6334), 155–159. https://doi.org/10.1126/science.aai8703
Wilson, A., & Kerswell, R. R. (2018). Can libration maintain Enceladus's ocean? *Earth and Planetary Science Letters*, *500*, 41–46.
Winslow, D. M., Fisher, A. T., & Becker, K. (2013). Characterizing borehole fluid flow and formation permeability in the ocean crust using linked analytic models and Markov chain Monte Carlo analysis. *Geochemistry, Geophysics, Geosystems*, *14*, 3857–3874. https://doi.org/10.1002/ggge.20241
Wisdom, J. (2004). Spin-orbit secondary resonance dynamics of Enceladus. *The Astronomical Journal*, *128*(1), 484.
Wu, P., & Peltier, W. R. (1982). Viscous gravitational relaxation. *Geophysical Journal of the Royal Astronomical Society*, *70*(2), 435–485. https://doi.org/10.1111/j.1365-246X.1982.tb04976.x
Zannoni, M., Hemingway, D., Casajus, L. G., & Tortora, P. (2020). The gravity field and interior structure of Dione. *Icarus*, 113713.
Zschau, J. (1978). Tidal friction in the solid Earth: Loading tides versus body tides. In *Tidal friction and the Earth's rotation* (pp. 62–94). Berlin, Germany: Springer.